Published text:

P M Evans, M A Mosleh-Shirazi, E J Harris, J Seco (2006)
Monte Carlo and Lambertian light guide models of the light output from scintillation crystals at megavoltage energies,
Medical Physics, Vol. 33(6), 1797-1809

Monte Carlo and Lambertian Light Guide Models of the Light Output from Scintillation Crystals at Megavoltage Energies

Philip M Evans, M Amin Mosleh-Shirazi[1], Emma J Harris and Joao Seco[2],

Joint Physics Department,

Institute of Cancer Research and Royal Marsden NHS Foundation Trust,

Downs Road, Sutton, Surrey, SM2 5PT, UK

Author for correspondence:

Philip Evans, Joint Physics Department, Royal Marsden Hospital, Downs Road, Sutton, Surrey, SM2 5PT, UK

Tel: + 44 208661 3349

Fax: + 44 208643 3812

Email: phil.evans@icr.ac.uk

Running title: Light output from scintillators

Number of pages: 37

Number of figures: 8

Number of tables: 1

Keywords:

radiation detectors, scintillation crystals, light output, electronic portal imaging

[1] Present address: Radiotherapy Department, Namazi Hospital, Shiraz University of Medical Sciences, Shiraz 71936-13311, Iran

[2] Present address: Francis H. Burr Proton Therapy Center, Massachusetts General Hospital, 30 Fruit Street, Boston MA, 02114, USA

Abstract

A new model of the light output from single crystal scintillators in megavoltage energy x-ray beams has been developed, based on the concept of a Lambertian light guide model (LLG). This was evaluated in comparison with a Monte Carlo (MC) model of optical photon transport, previously developed and reported in the literature, which was used as a gold standard. The LLG model was developed to enable optimization of scintillator detector design. In both models the dose deposition and light propagation were decoupled, the scintillators were cuboids, split into a series of cells as a function of depth, with Lambertian side and entrance faces, and a specular exit face. The signal in a sensor placed 1 mm and 1000 mm beyond the exit face was calculated. Cesium iodide crystals of 1.5 and 3 mm square cross section and 1, 5 and 10 mm depth were modeled. Both models were also used to determine detector signal and optical gain factor as a function of CsI scintillator thickness, from 2 to 10 mm. Results showed a variation in light output with position of dose deposition of a factor of up to approximately 5, for long, thin scintillators (such as 10 by 1.5 by 1.5 mm^3). For short fat scintillators (such as 1 by 3 by 3 mm^3) the light output was more uniform with depth. MC and LLG generally agreed to within 5%. Results for a sensor distance of 1mm showed an increase in light output the closer the light originates to the exit face, whilst a distance of 1000 mm showed a decrease in light output the closer the light originates to the exit face. For a sensor distance of 1 mm, the ratio of signal for a 10 mm scintillator to that for a 2 mm scintillator was 1.98, whereas, for the 1000 mm distance, the ratio was 3.00. The ratio of quantum efficiency (QE) between 10 mm and 2 mm thicknesses was 4.62. We concluded that these models may be used for detector optimization, with the light guide model suitable for parametric study.

I. Introduction

Scintillators are used in many medical x-ray imaging applications. Their high light yield and high density make them ideal for applications involving imaging megavoltage energy x-rays, such as radiotherapy treatment beams[1-11], diagnostic energy imaging[12,13], nuclear medicine[14,15], and dosimetry with plastic scintillators[16,17]. The relationship between x-ray energy deposition in the scintillator and signal in a sensor depends on the spatial characteristics of energy deposition, the probability of light creation from this energy distribution, the transport of the optical photons within the scintillator and their probability of reaching the sensor. The sensor is a device which forms an image with light collected from the scintillator and may be an amorphous silicon flat panel imager[12,18-22] or a camera[3,6-8,23].

In radiotherapy applications, the bremsstrahlung beam to be imaged is polychromatic, with a mean energy of typically between 1 and 8 MeV, with a component as low as 50-100 keV[24]. Thus different components of the x-ray spectrum may yield different optical signals in the sensor per unit of input x-ray energy, due to variation in the penetration of the various x-ray energies.

An important new area of radiation therapy is image-guided radiotherapy (IGRT). Imaging approaches include electronic portal imaging (EPI)[25,26], kilovoltage cone-beam CT (CBCT)[27], megavoltage CT (MVCT)[1,2,6,7,9,28,29] and kilovoltage fluoroscopy[30]. This involves an x-ray dose often to tissues outside the target. Additionally the lower the dose needed to form a useable image, the more efficient an IGRT intervention will be, or for a given dose, the better the photon statistics in the image will be. Hence there is the need to optimize imaging systems for use in IGRT.

In this paper we consider the modeling and optimization of the light output from single crystal scintillators. A new model is presented based on a Lambertian light guide (LLG) model, defined as a light guide with Lambertian side faces (Section IIC). The results of the new model are compared with the results of a Monte Carlo (MC) model we presented previously[6] (IIB), with the MC model taken as the gold standard (since it was in good agreement with experimental measurement[6]). The reason for developing the LLG model was to determine how fast and accurate an analytically based model could be in relation to the existing MC model. The LLG model involves numerical integration and the accuracy and CPU time requirements are determined by the number of elements used in this integration (IID). The dependency of these parameters was evaluated in comparison with the MC model.

The light output as a function of depth in the scintillation crystal is modeled and combined with the energy absorption characteristics of x-ray beams to yield signals in a sensor in close proximity to the exit face (1mm away, corresponding to a flat panel electronic portal imaging device, EPID) and remote from the exit face of the scintillator (1000 mm away corresponding to a camera based EPID). Two applications to calculating the signal for varying parameters are discussed: calculation for a given scintillator dimension for different x-ray spectra (IIE); and for studying effects of variations in detector thickness for a given spectrum (IIF). Effects on imaging performance are also considered (IIG). Results are presented for cesium iodide (CsI) and for megavoltage energy radiotherapy beams, although this approach is readily applicable to other scintillator materials and is expected to be valid for the kilovoltage energy range.

II. Methods

A. X-ray and Optical Photon Modeling

In this work we decoupled the transport of x-rays and optical photons. Hence in the models presented below, one Monte Carlo model was used to model ionizing radiation transport and another Monte Carlo (see section IIB) or the LLG (section IIC) model was used to describe light transport.

The system modeled is shown schematically in figure 1a. The scintillation crystal was modeled as a cuboid (or rectangular parallelepiped) with equal width and length sides. X-rays were normally incident on the entrance face. Calculations in the scintillator were split in the depth direction into 10 or 20 cells. X-ray dose deposition in each cell was modeled. The amount of light produced in each cell per incident x-ray was assumed proportional to energy deposited. Light transport was modeled and used to determine how many optical photons reach a sensor placed at an arbitrary distance, in air, outside the exit face opposite to the entrance face. This was done using the MC and LLG models described below, with the previously published MC model[6] taken as the gold standard and the LLG model evaluated in comparison. In both models, the entrance face of the cuboid and four side faces were described as being Lambertian (i.e. a diffuse surface with luminous intensity proportional to the cosine of the angle of emission) and the exit face as a polished, specular plane. This set of face characteristics was chosen on the basis of our previous work which showed that a two-dimensional array of scintillators with these characteristics may be constructed and produces a high light output[6]. Attenuation in the surfaces and volume and Fresnel refraction at the exit face of the crystal were modeled. Cells were numbered from 1 at

the exit face to N_{cell} at the entrance face. It was assumed the sides of the crystals are optically isolated.

The x-ray dose deposited in cell *N* per incident x-ray is defined as *d(N)*. The number of optical photons produced in cell *N* by this dose (the light yield) is *y(N)*. *y(N)* was determined by multiplying *d(N)* by the product of the mass of the cell, *m*, and the light yield per unit of x-ray energy absorbed, *g*. *g* is given by a stochastic distribution. These optical photons are then transported through the system until they are either absorbed or pass through the exit face. If they pass through the exit face and reach the sensor, they are detected and produce a signal *s(N)*. We define $\eta(N)$ as the percentage of optical photons launched in cell *N* that contribute to *s(N)*. Thus $\eta(N)$ is a measure of the optical efficiency of the system and *s(N)* may be given by:

$$s(N) = d(N)\, m\, g\, \eta(N) = y(N)\eta(N) \tag{1}$$

In Eq. 1, the term *d(N)* is given by the depth dose curve of the x-ray beam, *m* is the mass per cell, *g* is characteristic of the scintillator and $\eta(N)$ must be calculated. We now present the two models for determining $\eta(N)$.

B. Monte Carlo (MC) Model

We have described this model previously[6], and it is not further developed here, hence a brief summary is presented here.

Optical photons were generated isotropically in the volume of each cell and transported as vectors, with stochastic attenuation within the crystal volume and at interfaces. The number of optical photons launched was scaled in proportion to the

volume of the scintillator. Each photon was transported through the scintillator with a probability of being attenuated over path length, l, given by:

$$p_{vol}(l) = 1 - \exp(-l / l_{OAL}) \quad (2)$$

where l_{OAL} is the optical attenuation length for the scintillator material.

When a photon reached one of the five Lambertian faces it was absorbed with constant probability, p_{surf}. If not absorbed then the diffusely reflected output photon was generated with angular distribution[6]:

$$p_{lam}(\theta) = \sin(2\theta) \quad (3)$$

Unpolarized light was assumed, as the optical photons were expected to undergo a large number of reflections, and so, at the exit face, the probability of reflection was calculated as the average of the Fresnel intensity reflection coefficients for polarized light parallel and perpendicular to the plane of incidence. The sensor was modeled as a circle of radius 2 cm, concentric with the scintillator, at distance d_{sensor} and the number of optical photons reaching the sensor was scored.

The user inputs to this model were: refractive index (for Fresnel reflection), dose distribution ($d(N)$), l_{OAL}, p_{surf}, light yield/MeV (g), scintillator width and depth dimensions, and d_{sensor}.

C. Lambertian Light Guide (LLG) Model

Scintillators are generally highly transparent to their characteristic light. In addition reflections from their side faces may help to channel the light towards a sensor. Thus they may be considered as being like a light guide and a scintillator with Lambertian sides may be considered to be a light guide with Lambertian faces.

Again we divide the light guide into cells (Fig. 1a). The parameters listed in Section IIB are used. Light propagation depends on the mean solid angle of each cell and the end faces subtended at the other cells and faces plus the angular distribution, which is isotropic initially (for optical photons created in the volume) and Lambertian for reflections from each of the non-exit faces.

Starting with isotropic light generation within each cell, an iterative matrix approach was used to model the transport of the optical photons. ϕ_K is a vector describing the distribution of optical photons with one element for each cell, plus the entrance face and the sensor. After the K'th order transport, ϕ_K is related to ϕ_{K-1} by:

$$\phi_1 = S_n \, P_{n,m}^{initial} \, \phi_0 \tag{4a}$$

$$\phi_K = S_n \, P_{n,m} \, \phi_{K-1} \tag{4b}$$

where ϕ_0 is the initial light distribution produced by x-ray interaction in the volume of the scintillator and $P_{n,m}$, $P_{n,m}^{initial}$ are matrices describing the probability of transport from cell m to cell n. $P_{n,m}^{initial}$ is different to $P_{n,m}$ as it describes the initial isotropic distribution of optical photons from x-ray absorption, whereas optical photons created later in the transport process are the result of Lambertian scattering from faces of the scintillator. S_n is a matrix describing probability of not being absorbed in the faces of cell n. As the exit face is specular, reflection from this may be modeled directly using the matrix $P_{n,m}$ as shown below:

$$\phi = \begin{pmatrix} \text{Entrance surface} \\ \text{Cell N}_{\text{cell}} \\ \vdots \\ \text{Cell 1} \\ \text{Sensor} \end{pmatrix} \tag{5}$$

If ϕ_0 is given unit intensity for cell *N* and zero for all other elements, then the value of the matrix element corresponding to the sensor position after a large number of iterations is the optical efficiency, i.e.:

$$\phi_{K\to\infty}(\text{Sensor}) = \eta(N) \tag{6}$$

In Eq. 5, cells are numbered with increasing distance from the sensor. A dashed line separates the entrance face from the volume of the scintillator and a solid line separates the sensor. S_n is a diagonal matrix:

$$S_n = \begin{pmatrix} (1-p_{surf}) & & \\ & I(1-p_{surf}) & \\ & & 1 \end{pmatrix} \tag{7}$$

where *I* denotes the identity matrix. Each element of $P_{n,m}$ is a product of volume attenuation, $V_{n,m}$, solid angle and angular distribution:

$$P_{n,m} = V_{n,m} \times \lambda_{n,m} \tag{8}$$

$$V_{n,m} = e^{-\bar{L}/L_{OAL}} \tag{9}$$

where $\bar{L}$ is the average path length from cell *m* to cell *n* (averaged over the surface area of both cells). $\lambda_{n,m}$ is the amount of light entering cell *n* from cell *m* minus that escaping by passing through into the next cell from *n* (Fig. 1b):

$$\lambda_{n,m} = C_{n,m} - C_{n+1,m} \tag{10}$$

$C_{n,m}$ is the probability of optical photons scattered from the faces of cell *m* reaching the entrance of cell *n*. In the case of the initial isotropic distribution, this may be calculated analytically from the expression for the solid angle in Cartesian coordinates:

$$4\pi C_{n,m}^{initial} = \Omega = \int_{-x_0}^{x_0}\int_{-y_0}^{y_0} \frac{z_{n,m}\,dx\,dy}{\left(x^2 + y^2 + {z_{n,m}}^2\right)^{3/2}} = \pi - 2\sin^{-1}\left[1 - \frac{2{x_0'}^2{y_0'}^2}{\left(1+{x_0'}^2\right)\left(1+{y_0'}^2\right)}\right]$$

$$x_0' = \frac{x_0}{z_{n,m}} \qquad (11)$$

$$y_0' = \frac{y_0}{z_{n,m}}$$

where the width and length of the scintillator are $2x_0$ and $2y_0$ and $z_{n,m}$ is the distance from the depth at which the light originates in cell m to the entrance of cell n. Two similar distributions were also needed: the probability of Lambertian reflection from the side face of cell m entering cell n and the probability for the two end faces:

$$4\pi C_{n,m}^{side} = \int_{-x_0}^{x_0}\int_{-y_0}^{y_0} \frac{4\,y\,z_{n,m}\,dx\,dy}{\left(x^2 + y^2 + {z_{n,m}}^2\right)^2}$$

$$4\pi C_{n,m}^{end} = \int_{-x_0}^{x_0}\int_{-y_0}^{y_0} \frac{4\,{z_{n,m}}^2\,dx\,dy}{\left(x^2 + y^2 + {z_{n,m}}^2\right)^2} \qquad (12)$$

These were calculated numerically using the trapezium rule. The dihedral symmetry of the rectangular x,y face meant that only one quadrant needed to be calculated. n_{trap} is the number of integration points in x and y (see Fig. 1c).

The probability of escape at the exit face of the scintillator following reflection from the side of cell m, f_m^{side}, was calculated using Fresnel's equations (assuming unpolarized light) averaged over the ${n_{trap}}^2$ points. The probability of escaping photons striking the detector sensor, d_m, was calculated as the solid angle subtended by the sensor at the exit face. Values of $C^{initial}$, C^{side} and C^{end} were averaged over the central plane of the cell, the side face and the end face respectively. The number of points for averaging was n_{ave} in each dimension (see Fig. 1c).

Consider light propagating from cell *m* to *n*. It may either travel directly between the cells, in which case the probability depends on the distance between them $|m\text{-}n|$, so the two subscripts *n,m* in Eqs. 4-12 may be replaced by one: *m-n* (for a scintillator with non-Lambertian sides, two subscripts might still be needed). Alternatively light from cell *m* may be reflected from the specular exit face (with a probability of escape from this face) and go back to cell *n.* The distance the light travels between the cells for this mirror process is *m+n-1* (the subscripts *n,m* in Eqs. 4-12 may be replaced by *m+n-1*). This process is illustrated in Fig. 1b, where the example of *m* set to 4 and *n* set to 2 is shown, with the distance traveled 2 cells for the direct case and 5 for the mirror case. Thus Eq. 10 may be split into two parts:

$$P_{n,m} = P^{direct}_{|n-m|} + P^{mirror}_{m+n-1}$$

$$P^{direct}_{|n-m|} = \left(\begin{array}{c:c:ccc:c} 0 & V_1^{ce}C_1^{side} & \cdots & \cdots & V_{Ncell}^{ce}C_{Ncell}^{side} & 0 \\ \hdashline V_1^{ce}\lambda_0^{side} & V_0^{cc}\lambda_0^{side} & V_1^{cc}\lambda_1^{side} & \ddots & V_{Ncell-1}^{cc}\lambda_{Ncell-1}^{side} & 0 \\ \vdots & V_1^{cc}\lambda_1^{side} & \ddots & \ddots & \ddots & \vdots \\ \vdots & \ddots & \ddots & \ddots & V_1^{cc}\lambda_1^{side} & \vdots \\ V_{Ncell}^{ce}\lambda_{Ncell-1}^{end} & V_{Ncell-1}^{cc}\lambda_{Ncell-1}^{side} & \ddots & V_1^{cc}\lambda_1^{side} & V_0^{cc}\lambda_0^{side} & 0 \\ \hline V_{Ncell}^{ee}C_{Ncell}^{end}f_{Ncell}^{end}d_{Ncell} & V_{Ncell}^{ce}C_{Ncell}^{side}f_{Ncell}^{side}d_{Ncell} & \cdots & \cdots & V_1^{ec}C_1^{side}f_1^{side}d_1 & 1 \end{array}\right)$$

$$P^{mirror}_{m+n-1} = \left(\begin{array}{c:c:ccc:c} V_{2Ncell}^{ee}C_{2Ncell}^{end}\alpha_{Ncell+1}^{f_{Ncell}^{end}} & V_{2Ncell}^{ce}C_{2Ncell}^{side}\alpha_{Ncell+1}^{f_{Ncell}^{side}} & \cdots & \cdots & V_{Ncell+1}^{ce}C_{Ncell+1}^{side}\alpha_{Ncell+1}^{f_1^{side}} & 0 \\ \hdashline V_{2Ncell}^{ce}\lambda_{2Ncell-1}^{end}\alpha_{Ncell}^{f_{Ncell}^{end}} & V_{2Ncell-1}^{cc}\lambda_{2Ncell-1}^{side}\alpha_{Ncell}^{f_{Ncell}^{side}} & V_{2Ncell-2}^{cc}\lambda_{2Ncell-2}^{side}\alpha_{Ncell}^{f_{Ncell-1}^{side}} & \iddots & V_{Ncell}^{cc}\lambda_{Ncell}^{side}\alpha_{Ncell}^{f_1^{side}} & 0 \\ \vdots & V_{2Ncell-2}^{cc}\lambda_{2Ncell-2}^{side}\alpha_{Ncell-1}^{f_{Ncell}^{side}} & \iddots & \iddots & \iddots & \vdots \\ \vdots & \iddots & \iddots & \iddots & V_2^{cc}\lambda_2^{side}\alpha_2^{f_1^{side}} & \vdots \\ V_{Ncell+1}^{ce}\lambda_{Ncell}^{end}\alpha_1^{f_{Ncell}^{end}} & V_{Ncell}^{cc}\lambda_{Ncell}^{side}\alpha_1^{f_{Ncell}^{side}} & \iddots & V_2^{cc}\lambda_2^{side}\alpha_1^{f_2^{side}} & V_1^{cc}\lambda_1^{side}\alpha_1^{f_1^{side}} & 0 \\ \hline 0 & 0 & \cdots & \cdots & 0 & 0 \end{array}\right)$$

(13)

where the *V* terms were calculated using Eq. 9, taking into account whether the distance was between a cell and another (V^{cc}), a cell and an end face (V^{ce}) or between two end faces (V^{ee}). The subscripts of λ, *C* and *V* are the modulus of *m-n*, ($|m\text{-}n|$), in P^{direct} and *m+n-1* in P^{mirror}. The right hand column is used to preserve the accumulated

signal in the sensor. λ_0 is equal to $1\text{-}2C_1$. The terms α^f_{cell} in P^{mirror} denote the probability of light that reaches the exit face, being reflected and reaching a given cell. The sum of α over each column is $(1\text{-}f)$ (see Fig. 1c). An analogous expression to Eq. 13 may be written for the initial isotropic distribution, with the first column elements all zero and the superscript *side* replaced with *initial*. The central region of P^{direct} has the Toeplitz structure characteristic of Markovian processes. Figure 2 shows example values of the C and f coefficients for from 1 to 20 cells.

Iterative equation 4 was used to calculate $\eta(N)$ as a function of starting cell number. 300 iterations were used leaving a residual signal in the scintillator of order 10^{-7}.

D. Choice of integration parameters in LLG model

User variable parameters are the number of cells N_{cell} and the integration parameters n_{ave} and n_{trap}. Previously we showed a N_{cell} value of 10 gave reasonable results[6]. Effects of n_{ave} and N_{cell} are linked. For a given scintillator length, the greater the value of N_{cell}, the closer spaced are the integration points for a given n_{ave}. Also the greater the cell aspect ratio, AR, (cell height over scintillator width), the larger the value of n_{ave} needed to sample the sides adequately. To determine the optimum value for n_{ave}, and for a given N_{cell}, the root mean square (RMS) difference between MC and LLG models (averaged over all cells) was determined for a range of cell AR values (Section IIH). Choice of n_{trap} is important when the sensor is placed at a large distance (e.g. 1000 mm), as the sensor presents a small solid angle to the exit face and a large enough value of n_{trap} is needed to ensure sufficient sampling is carried out in the sensor.

E. Signal Calculation for X-ray Spectra

The decoupling of x-ray and optical photon calculations means that various x-ray beams may be modeled without the need to recalculate optical photon transport, as the optical efficiency, $\eta(N)$, may be precalculated. In addition the relationship between dose (and hence energy absorbed) and depth of a range of mono-energetic beams, $d_E(N)$, may be precalculated (E denotes energy). For each energy, the average optical efficiency, $\overline{\eta}_E$, may be calculated:

$$\overline{\eta}_E = \frac{\sum_N \eta(N) d_E(N)}{\sum_N d_E(N)} \tag{14}$$

For a polychromatic beam, of fluence distribution ψ_E, the average optical efficiency, $\overline{\eta}_{beam}$, is:

$$\overline{\eta}_{beam} = \frac{\sum_E \overline{\eta}_E \Psi_E}{\sum_E \Psi_E} \tag{15}$$

The EGSnrc usercode DOSRZnrc[31,32] was used to determine the dose $d_E(N)$, for a range of monochromatic x-ray energies, E. Data for polychromatic beams were generated by summing over the spectrum. For all DOSRZnrc calculations, 10^7 x-ray histories were modeled and a beam radius of 0.1 cm was used. The standard deviation on the dose calculated was typically 0.5% and no greater than 1.0%.

F. Optimization of Scintillator Thickness

Varying the scintillator thickness may be used to study detector optimization. Increasing thickness will increase quantum efficiency, but may diminish optical efficiency and optical Swank factor. In the MC model, investigation of scintillator

thickness dependence requires a new calculation for each case. In the LLG model, the coefficients may be calculated once for the longest scintillation crystal to be considered and a subset of the coefficients reused to model shorter scintillators using fewer component cells, e.g. coefficients for 20 x 0.5 mm cells, may also be used for thicknesses that are integer multiples of 0.5 mm up to 10 mm.

G. Effects on Detective Quantum Efficiency

The conversion of x-rays into optical photons in the scintillator is a stochastic process and hence g, in Eq. 1, will vary about its mean value from x-ray photon to photon and add noise to the final signal[33,34]. We assume this variation follows a Poisson distribution. We denote s_{abs} as the number of optical photons detected per x-ray absorbed (also a Poisson distribution by this assumption). X-ray energy deposition in the scintillator will vary from x-ray photon to photon. This will constitute an extra source of noise which will not follow Poisson statistics[35]. We neglect this in this work.

Quantum efficiency, *QE*, is given by:

$$\mathrm{QE} = 1 - \exp\left(-\overline{\mu} t\right) \tag{16}$$

with t the thickness and $\overline{\mu}$ the average attenuation coefficient over the 6 MV spectrum. s_{abs} is given by:

$$s_{abs} = \frac{\sum_N d(N) m}{QE} g \overline{\eta}_{beam} \tag{17}$$

Detective quantum efficiency[33,34], *DQE*, is:

$$\mathrm{DQE} = \mathrm{QE}\left(1 + \frac{1}{s_{abs}}\right)^{-1} \tag{18}$$

320

H. Parameters Studied

The scintillator material modeled was cesium iodide, CsI. Parameters were taken from previous work[6]: density, ρ, was 4.51 g/cm^3, refractive index was 1.8, g was 56000 photons/MeV, l_{OAL} was 1000 mm and p_{surf} was 0.07.

325

Scintillation crystal widths modeled were 1.5 and 3 mm. Crystal depths of 1, 5 and 10 mm were used. d_{sensor} was 1 mm and 1000 mm, both in air (to model the worst optical coupling case). 1 mm distance corresponds to a detector in close contact such as an amorphous silicon panel and 1000 mm distance corresponds to a camera EPID. For
330 this case, a lens radius of 20 mm was modeled, with angular subtense of 1.15°.

For the first study, the results for the LLG model were compared, with the MC model as reference (since it was compared with experimental data[6]). This allowed determination of suitable values of n_{ave} and n_{trap} (see IID) to give RMS agreement
335 with the MC model of 5%. N_{cell} was 10 and the RMS difference was determined as a function of AR. In addition the dependence on n_{trap} was studied for the scintillator of 10 mm depth by 1.5 mm by 1.5 mm, with n_{ave} and N_{cell} set to 21 and 10. Results were then analyzed cell by cell for 10 cells (20 cells in case of large discrepancy) and for all scintillator sizes. In the second study, signal calculation for x-ray spectra was
340 investigated for a polychromatic 6 MV spectrum[24]. A third study investigated the optimization of crystal thickness. This was done using coefficients for 20 cells in the LLG model. 10 cells were used for each thickness in the MC model. Finally the effects of optical photon collection on DQE were studied.

III. Results and Discussion

A. Comparison of Monte Carlo and Lambertian Light Guide Models

Figure 3a shows the RMS difference between LLG and MC models as a function of AR. Data are shown for n_{trap} equals 100 and 800 for d_{sensor} values of 1 and 1000 mm respectively and a n_{ave} value of 21. Data for a d_{sensor} value of 1 mm show a rise with AR, because for large AR the n_{ave} points along the side of the cell are not sufficient to ensure good sampling. For d_{sensor} equals 1000 mm the data are essentially flat. Arrows show the effect of number of cells for 10 by 1.5 by 1.5 mm^3, with 10 cells at the arrow tail (AR is 0.67) and 20 cells (AR is 0.33) at the arrow head. The results for a d_{sensor} value of 1 mm are improved, whereas those for 1000 mm are not. Fig. 3b shows the RMS difference as a function of n_{trap} for n_{ave} equals 21 and d_{sensor} equals 1000 mm. RMS difference decreases with n_{trap} until a value of 800, then levels off at a finite value limited by the numerical integration. This is a consequence of the need for sufficient sampling points in a 20 mm radius sensor, at 1000 mm distance to contribute to the signal in the sensor (see Fig. 1c). Data for d_{sensor} equals 1 mm (not presented) shows a much weaker dependence. We conclude values of: 10 cells, 21 for n_{ave} and 100 (small d_{sensor}) or 800 (large d_{sensor}) for n_{trap} are adequate. For long, thin crystals (AR above 0.33) larger n_{ave} or more cells are needed.

Figure 4a shows light collection efficiency, $\eta(N)$, as a function of cell number where light originated, N, for d_{sensor} equals 1 mm. N_{cell} is 10. The lines are labeled "depth × width × length". The number of histories for the MC model was $10^5/mm^3$, giving a statistical error of under 1%. Figure 4b shows calculations for d_{sensor} equals 1000 mm. The lower light collection efficiency for this case meant more histories, 10^7, were needed for the MC (for 1% error). The results show (in the context of the assumptions

made and systems modeled in this study) the average optical efficiency decreases with increased scintillator thickness. This is because as thickness increases there is greater chance of absorption in the side faces. For long thin scintillators, there is a variation in signal with depth. For the sensor close to the exit face, the signal increases, as the optical photons are created closer to the exit, mainly due to the lower probability of absorption in the side faces before escaping. For d_{sensor} equals 1000 mm, the lens subtends 1.15° and so the angle of incidence must be below 0.57°. Scattering from the Lambertian side and entrance faces helps to produce optical photons with the necessary trajectory to exit the scintillator and reach the lens. Thus a channeling effect is produced. Optical photons launched far from the exit face have a greater probability of scattering at the side and entrance faces with the necessary trajectory to escape and reach the sensor. Thus Figs. 4b shows the opposite trend to Figs. 4a. The data for 10 by 3 by 3 and 5 by 1.5 by 1.5, which have the same shape but different scale, almost perfectly overlap. This is because the volume attenuation is negligible for this size.

Figures 5a and 5b shows the percentage deviation of the LLG results from the MC results in Fig. 4. All are within 5% for 5a, except the 10 by 1.5 by1.5 case. A smaller deviation was obtained with an N_{cell} of 20 (with the results of adjacent cells averaged to produce data at 10 points). For 5b, the errors between MC and LLG are smaller than 10% for the majority of points. Table 1 shows statistics for the comparison between the two models. RMS agreement is within 5% in all cases and of order 1% for the d_{sensor} equals 1 mm situation. The larger errors for the 1000 mm d_{sensor} case are a result of the small solid angle ($3x10^{-4}$ steradians) subtended by the sensor as discussed above.

B. Signal Calculation for X-ray Spectra

Modeling a polychromatic x-ray spectrum is illustrated in figure 6. Fig. 6a shows normalized dose as a function of x-ray energy and depth in the crystal for a 10 by 3 by 3 mm^3 scintillator. Fig. 6b shows the result of multiplying the data in 6a by the optical efficiencies from the LLG model in Fig. 4, from Eq. 14. Optical efficiency is flat as a function of energy for short, fat crystals. For long, thin crystals, the data show two flat regions for low and high energies joined by a transition region at 0.1-0.5 MeV. Fig 6a shows that this energy range corresponds to a transition from most dose being deposited close to the entrance to a more uniform distribution with depth. In the attenuation coefficient of CsI this energy range corresponds to the transition from photoelectric effect to Compton scattering as the dominant interaction mechanism. Fig. 6c shows the result of a weighted summation of 6b over the 6 MV spectrum for a crystal cross-sectional area of 3 by 3 mm^2 and all three depths, from Eq. 15. As expected the value of d_{sensor} is the main determinant of optical efficiency, which also decreases as the crystal thickness increases, as expected from Fig. 4. The decoupling of the x-ray and optical photon transport allows calculation of the detector signal without remodeling the optical component for each x-ray beam.

This calculation assumes the relationship between incident x-ray energy and light yield is linear. Literature suggests there is a deviation from linearity for low energies, particularly close to the K and L edges[36], with an over-response of 10 to 15%. This effect could be incorporated into the model with an energy dependent $\eta(N)$ in Eq. 14.

C. Optimization of Scintillator Thickness

Figure 7a shows $\eta(N)$ for a range of scintillation crystal thicknesses and with d_{sensor} equals 1 mm. For the LLG model, each cell has cross-sectional area 1.5 by 1.5 mm^2 and depth 0.5 mm. Data for 4 to 20 cells are shown (thicknesses of 2 mm to 10 mm). MC data were generated for 10 cells for all thicknesses. Fig. 7b shows results for d_{sensor} equals 1000 mm. MC calculations are shown for integer thickness in mm. The cross symbols, close to the 2 mm data, in Fig. 7a show the LLG results for 2 mm thickness and 10 cells. Agreement with MC is now better suggesting that the discrepancy for 2 mm thickness is due to the small number of cells (5) used in the LLG calculation for this thickness.

The behavior in Fig. 7 follows that seen in Fig. 4, with optical efficiency showing a decrease with increasing scintillator length (due to an increased probability of absorption in the crystal faces), a decrease with distance from the exit face for a d_{sensor} value of 1 mm (due to the increased probability of escape with proximity to the exit face), and an increase for 1000 mm (due to the increased probability of escaping after being scattered and traveling towards the sensor).

D. Effects on Detective Quantum Efficiency

Figures 8a and 8b show the use of the LLG model data in Fig. 7 to calculate $\overline{\eta}_{beam}$, s, s_{abs}, QE and DQE for the 6 MV beam. Analysis of the data presented in Fig. 8a showed that the ratio of signal for a 10 mm scintillator to that for a 2 mm scintillator (open squares joined by dotted line), $S_{10/2}$, was 1.98 whereas the ratio of quantum efficiency (solid squares joined by solid line), $QE_{10/2}$, was 4.62, indicating a decrease in percentage light signal as scintillator thickness is increased. For Fig. 8b, the values show a similar behavior, with $S_{10/2}$ equal to 3.00. The results in Fig. 8a also show that,

as expected, if most of the exiting light is collected (i.e. s_{abs} is large), then the effect of the noisy gain is small and DQE is equal to QE. In 8b, the effects of low optical photon collection efficiency produce a significant effect on DQE, as shown by the separation of the QE and DQE lines. The simplifying assumptions made in generating Fig. 8 should be remembered, i.e. the variation in energy deposited per x-ray has been neglected.

E. Computer Timings

All calculations were carried out on an IBM blade computer with two 2.8 GHz Xeon CPUs. For the data in Figs. 4a and 5a, the MC model required 8 minutes and the LLG model required 16 and 31 minutes (for 10 and 20 cells respectively) for each crystal. The data in Figs. 4b and 5b required 16 hours for both optical photon transport models. The data in Fig. 7 for calculating light yield as a function of scintillator thickness required 45 and 91 min in 7a and 63 and 95 hours in 7b for LLG and MC models, respectively. The CPU time required by the LLG is dominated by the numerical integrations in Eq. 12. Good analytical approximations to these expressions, along the lines of Eq. 11 would speed up this model considerably and yield significant benefit over the MC model.

F. Context to Other Work

Several authors have studied the dose response of imaging systems used at high x-ray energy. These studies have generally considered ionizing radiation transport only and/or phosphor screens, containing polycrystalline gadolinium oxysulfide. Jaffray et al.[37] calculated absorbed energy distributions for a range of gadolinium oxysulfide thicknesses and energies using MC. Other authors have generated MC based

dosimetric models of complete EPIDs[38,39]. Radcliffe et al.[40] presented a MC model of the light output from gadolinium oxysulfide screens. This model described optical transport assuming the screen to be a weakly absorbing medium, with scattering due to Fresnel reflection and refraction at the boundaries between the binder and the phosphor grains. Bissonnette et al.[41] used the average optical photon yield from Radcliffe et al. in a model of video based EPIDs. This was further used to develop a model to determine optimal phosphor thickness[35]. Badano and colleagues[42-44] have used the Detect-II optical Monte Carlo system to model light transport in imaging systems. Systems studied include columnar CsI crystal arrays in kV beams[44].

V. Conclusions

Two models for calculating the light output from scintillators crystals have been compared. One is a Monte Carlo (MC) simulation of optical photon transport, previously presented. The other is a description of a light guide with Lambertian faces (LLG). The LLG model generally agrees to within 5% with the MC model. Results show a variation in light output with position of dose deposition and with scintillator length of typically a factor of two. Both models may be used to determine the variation in detector signal as a function of detector thickness and thus they are suited to detector optimization. The LLG model provides physical insight in that the macroscopic nature of the LLG model emphasizes the importance of basic geometric considerations in determining the light yield in the sensor.

References

[1]R. G. Simpson, C. T. Chen, E. A. Grubbs and W. Swindell, “A 4-MV CT scanner for radiation therapy: the prototype system,” Med. Phys. **9**, 574-579 (1982).

[2]A. Brahme, B. Lind and P. Näfstadius, “Radiotherapeutic computed tomography with scanned photon beams,” Int. J. Radiat. Oncol. Biol. Phys. **13**, 95-101 (1987).

[3]S. A. Watson, T. Kaupilla, B. Haight and K. Mueller, “Multiframe, high-energy, radiographic cameras for submicrosecond imaging,” Los Alamos National Laboratory report, LA-UR-95-3570 (1995).

[4]J. P. Bissonnette and P. Munro, “Evaluation of a high-density scintillating glass for portal imaging,” Med. Phys. **23**, 401-406 (1996).

[5]J. R. N. Symonds-Tayler, M. Partridge and P. M. Evans, “An electronic portal imaging device for transit dosimetry,” Phys. Med. Biol. **42**, 2273-2283 (1997).

[6]M. A. Mosleh-Shirazi, W. Swindell and P. M. Evans, “Optimization of the scintillation detector in a combined 3D megavoltage CT scanner and portal imager,” Med. Phys. **25**, 1880-1890 (1998).

[7]M. A. Mosleh-Shirazi, P. M. Evans, W. Swindell, S. Webb and M. Partridge, “A cone-beam megavoltage CT scanner for treatment verification in conformal radiotherapy, Radiother. Oncol. **48**, 319-328 (1998).

[8]A. Sawant, H. Zeman, S. Samant, G. Lovhoiden, B. Weinberg, and F. DiBianca, “Theoretical analysis and experimental evaluation of a CsI(Tl) based electronic portal imaging system," Med. Phys. **29**, 1042-1053 (2002).

[9]E. J. Seppi, P. Munro, S. W. Johnsen, E. G. Shapiro, C. Tognina, D. Jones, J. M. Pavkovich, C. Webb, I. Mollov, L. D. Partain and R. E. Colbeth, “Megavoltage cone-beam computed tomography using a high-efficiency image receptor,” Int. J. Radiat. Oncol. Biol. Phys. **55**, 793-803 (2003).

[10]T. T. Monajemi, S. Steciw, B. G. Fallone, and S. Rathee, “Modeling scintillator-photodiodes as detectors for megavoltage CT," Med. Phys. **31**, 1225-1234 (2004).

[11]A. Sawant, L. E. Antonuk, Y. El-Mohri, Y. Li, Z. Su, Y. Wang, J. Yamamoto, Q. Zhao, H. Du, J. Daniel, and R. Street, “Segmented phosphors: MEMS-based high quantum efficiency detectors for megavoltage x-ray imaging," Med. Phys. **32**, 553-565 (2005).

[12]L. E. Antonuk, K.-W. Jee, Y. El-Mohri, M. Maolinbay, S. Nassif, X. Rong, Q. Zhao, J. H. Siewerdsen, R. A. Street, and K. S. Shah, “Strategies to improve the signal and noise performance of active matrix, flat-panel imagers for diagnostic x-ray applications,” Med. Phys. **27**, 289-306 (2000)

[13]W. Zhao, G. Ristic, and J. A. Rowlands, “X-ray imaging performance of structured cesium iodide scintillators," Med. Phys. **31**, 2594-2605 (2004).

[14]R. J. Ott, “Position sensitive detectors for medical imaging,” Nucl. Instrum. Methods A **392**, 396-401 (1997).

[15]C. W. E. van Eijk, “Inorganic scintillators in medical imaging,” Phys. Med. Biol. **47**, R85-R106 (2002).

[16]D. Fluhs, M. Heintz, F. Indenkampen, C. Wieczorek, H. Kolanoski, and U. Quast U, “Direct reading measurement of absorbed dose with plastic scintillators - The general concept and applications to ophthalmic plaque dosimetry,” Med. Phys. **23,** 427-434 (1996).

[17]A. S. Beddar, T. M. Briere, F. A. Mourtada, O. N. Vassiliev, H. H. Liu, and R. Mohan, “Monte Carlo calculations of the absorbed dose and energy dependence of plastic scintillators,” Med. Phys. **32,** 1265-1269 (2005).

[18]L. E. Antonuk, J. Yorkston, W. Huang, H. Sandler, J. H. Siewerdsen and Y. El-Mohri, “Megavoltage imaging with a large-area, flat-panel, amorphous silicon imager,” Int. J. Radiat. Oncol. Biol. Phys. **36**, 661-672 (1996).

[19]G. Pang and J. A. Rowlands, "Development of high quantum efficiency flat panel detectors for portal imaging: Intrinsic spatial resolution," Med. Phys. **29**, 2274-2285 (2002).

[20]P. B. Greer and C. C. Popescu, "Dosimetric properties of an amorphous silicon electronic portal imaging device for verification of dynamic intensity modulated radiation therapy," Med. Phys. **30**, 1618-1627 (2003).

[21]L. N. McDermott, R. J. W. Louwe, J.-J. Sonke, M. B. van Herk, and B. J. Mijnheer, "Dose–response and ghosting effects of an amorphous silicon electronic portal imaging device," Med. Phys. **31**, 285-295 (2004).

[22]J. V. Siebers, J. O. Kim, L. Ko, P. J. Keall, and R. Mohan, "Monte Carlo computation of dosimetric amorphous silicon electronic portal images," Med. Phys. **31**, 2135-2146 (2004).

[23]J. C. J. deBoer, B. J. M. Heijmen, K. L. Pasma and A. G. Visser, “Characterisation of a high-elbow fluoroscopic electronic portal imaging device for portal dosimetry,” Phys. Med. Biol. **45**, 197-216 (2000).

[24]S. Flampouri, P. M. Evans, F. Verhaegen, A. E. Nahum, E. Spezi and M. Partridge, “Optimisation of accelerator target and detector for portal imaging using Monte Carlo simulations and experiment,” Phys. Med. Biol. **47,** 3331-3349 (2002).

[25]M. G. Herman, J. M. Balter, D. A. Jaffray, K. P. McGee, P. Munro, S. Shalev, M. van Herk, and J. W. Wong, "Clinical use of electronic portal imaging: Report of AAPM Radiation Therapy Committee Task Group 58," Med. Phys. **28**, 712-737 (2001).

[26]L. E. Antonuk, "Electronic portal imaging devices: a review and historical perspective of contemporary technologies and research," Phys. Med. Biol. **47**, R31-R65 (2002).

[27]D. A. Jaffray, J. H. Siewerdsen, J. W. Wong and A. A. Martinez, "Flat-panel cone-beam computed tomography for image-guided radiation therapy," Int. J. Radiat. Oncol. Biol. Phys. **53**, 1337-1349 (2002).

[28]E. C. Ford, J. Chang, K. Mueller, K. Sidhu, D. Todor, G. Mageras, E. Yorke, C. C. Ling, and H. Amols, "Cone-beam CT with megavoltage beams and an amorphous silicon electronic portal imaging device: Potential for verification of radiotherapy of lung cancer," Med. Phys. **29**, 2913-2924 (2002).

[29]J. Pouliot, A. Bani-Hashemi, J. Chen, M. Svatos, F. Ghelmansarai, M. Mitschke, M. Aubin, P. Xia, O. Morin, K. Bucci, M. Roach III, P. Hernandez, Z. Zheng, D. Hristov, and L. Verhey, "Low-dose megavoltage cone-beam CT for radiation therapy," Int. J. Radiat. Oncol. Biol. Phys. **61**, 552-560 (2005).

[30]R. Onimaru, H. Shirato, H. Aoyama, K. Kitakura, T. Seki, K. Hida, K. Fujita, K. Kagei, T. Nishioka, T. Kunieda, Y. Iwasaki, and K. Miyasaka, "Calculation of rotational setup error using the real-time tracking radiation therapy (RTRT) system and its application to the treatment of spinal schwannoma," Int. J. Radiat. Oncol. Biol. Phys. **54**, 939-947 (2002).

[31]I. Kawrakow, "Accurate condensed history Monte Carlo simulation of electron transport: I. EGSnrc, the new EGS4 version," Med. Phys. **27**, 485-498 (2000).

[32]I. Kawrakow, "Accurate condensed history Monte Carlo simulation of electron transport. II. Application to ion chamber response simulations," Med. Phys. **27**, 499-513 (2000).

[33]H. H. Barrett and W. Swindell, *Radiological imaging*, (Academic, San Diego, CA, 1981), pp. 285-289.

[34]R. K. Swank, "Absorption and noise in x-ray phosphors," J. Appl. Phys. **44**, 4199-4203 (1973).

[35]J. P. Bissonnette, I. A. Cunningham, and P. Munro, "Optimal phosphor thickness for portal imaging," Med. Phys. **24**, 803-814 (1997).

[36]W. Mengesha, T.D. Taulbee, B.D. Rooney and J.D. Valentine, "Light yield nonproportionality of CsI(Tl), CsI(Na) and YAP," IEEE Transactions on Nucl. Sci. **45**, 456-461 (1998).

[37]D. A. Jaffray, J. J. Battista, A. Fenster, and P. Munro, "Monte Carlo studies of x-ray energy absorption and quantum noise in megavoltage transmission radiography," Med. Phys. **22**, 1077-1088 (1995).

[38]E. Spezi and D. G. Lewis, "Full forward Monte Carlo calculation of portal dose from MLC collimated treatment beams," Phys. Med. Biol. **47**, 377-390 (2002).

[39]C. Kirkby and R. Sloboda, "Consequences of the spectral response of an a-Si EPID and implications for dosimetric calibration," Med. Phys. **32**, 2649-2658 (2005).

[40]T. Radcliffe, G. Barnea, B. Wowk, R. Rajapakshe, and S. Shalev, "Monte Carlo optimization of metal/phosphor screens at megavoltage energies," Med. Phys. **20**, 1161-1169 (1993).

[41]J. P. Bissonnette, I. A. Cunningham, D. A. Jaffray, A. Fenster, and P. Munro, "A quantum accounting and detective quantum efficiency analysis for video-based portal imaging," Med. Phys. **24**, 815-826 (1997)

[42]A. Badano, R. M. Gagne, B. D. Gallas, R. J. Jennings, J. S. Boswell, and K. J. Myers, **"**Lubberts effect in columnar phosphors," Med. Phys. **31**, 3122-3131 (2004).

[43]B. D. Gallas, J. S. Boswell, A. Badano, R. M. Gagne, and K. J. Myers, "An energy- and depth-dependent model for x-ray imaging," Med. Phys. **31**, 3122-3131 (2004).

[44]A. Badano and J. Sempau, **"**MANTIS: combined x-ray, electron and optical Monte Carlo simulations of indirect radiation imaging systems," Phys. Med. Biol. **51**, 1545-1561 (2006).

Acknowledgements

This work is support by Cancer Research UK under Program Grant C46/A3970. We are grateful to Andrew Fielding, Mike Partridge and Will Ryder for useful discussions during the course of this work.

Table Caption

Table 1: Values of difference in $\eta(N)$ between LLG and MC models for the six scintillator dimensions studied and for the two values of d_{sensor}. 'max' denotes the maximum absolute error value and 'RMS' denotes root mean square error.

610 **Table 1**

Cell Dimensions (mm^3)	d_{sensor} equals 1 mm		d_{sensor} equals 1000 mm	
	max (%)	RMS (%)	max (%)	RMS (%)
1 by 3 by 3	0.74	0.31	9.94	4.79
1 by 1.5 by 1.5	0.73	0.33	13.15	4.50
5 by 3 by 3	0.32	0.21	10.56	3.78
5 by1.5 by 1.5	1.75	1.01	5.51	4.16
10 by 3 by 3	1.47	0.89	6.07	3.93
10 by 1.5 by 1.5	7.21	4.40	7.68	4.39
10 by 1.5 by 1.5 (20 cells)	3.36	2.03	6.01	3.70

Figure Captions

Figure 1: Illustration of the multicell model. a) 3D representation of x-rays incident on the entrance face of the scintillator from above, showing cell labeling scheme and propagation of optical photons to the sensor. b) illustration of calculation of transport from point *P* in cell *m* to surfaces points in cell *n* in the LLG model. The number of photons interacting in cell *n* is equal to the number entering minus number passing though (shown by the 4 arrows for "Direct"). "Direct" shows component from *m* to *n*. "Mirror" shows component from reflection at exit face. c) illustration of integration parameters n_{ave} and n_{trap} in the LLG model. $\alpha_n^{f_m^{side}}$ is the probability of optical photon starting at the side face of *m*, reflecting from the exit face and reaching *n*.

Figure 2: Values of the coefficients $C^{initial}$, C^{side}, C^{end}, $f^{initial}$, f^{side}, f^{end} in the LLG model as a function of cell number, for 20 component cells of width and length 1.5 mm and depth 0.5 mm. The x axis is $|n\text{-}m|$. Lines are to aid the eye.

Figure 3: Illustration of the dependency of the model parameters, N_{cell}, n_{ave} and n_{trap} on the RMS error of the LLG model results compared to the MC model. a) shows results as a function of cell aspect ratio (AR) with n_{ave} equals 21, and n_{trap} equals 100 and 800 for d_{sensor} values of 1 mm (solid circles) and 1000 mm (open squares) respectively. Data are shown for N_{cell} equals 10, except the larger symbols at the heads of the arrows, for which N_{cell} is 20. b) shows results for n_{ave} equals 21 and d_{sensor} equals 1000 mm as a function of n_{trap}.

Figure 4: Optical efficiency, $\eta(N)$, as a function of cell number where light originates for six CsI scintillator sizes. MC model results are shown as crosses joined by solid lines, to aid the eye, and LLG model results as open symbols joined by dashed lines. a) d_{sensor} equals 1 mm. b) d_{sensor} equals 1000 mm.

Figure 5: Percentage difference between MC and LLG models for a) d_{sensor} equals 1 mm. b) d_{sensor} equals 1000 mm. In a) "10x1.5x1.5 (20 cells)" denotes calculation using 20 cells for LLG and averaging to yield results for 10 cell. The solid lines at plus and minus 1% show the standard deviation of the MC calculations.

Figure 6: a) DOSRZnrc calculations of dose per cell as a function of x-ray energy in MeV, *E*, and depth for a 10 by 3 by 3 mm^3 CsI scintillator, and 10 cells. Results are normalized for each energy to unit area under each curve. b) optical efficiency as a function of x-ray energy, summed over all cells, $\overline{\eta}_E$, determined using the LLG model. Solid symbols show results for d_{sensor} equals 1 mm (left hand y axis) and open symbols for d_{sensor} equals 1000 mm (right hand y axis). The lines are to aid the eye. c) results of a weighted sum of 6b over an example 6 MV spectrum, $\overline{\eta}_{beam}$, for CsI scintillators of 3 by 3 mm^2 cross-section and 1, 5 and 10 mm depth.

Figure 7: Optical efficiency, $\eta(N)$, as a function of distance from exit face for a series of CsI scintillator thicknesses from 2 mm to 10 mm and 1.5 by 1.5 mm^2 cross section. In a) d_{sensor} is 1 mm and in b) d_{sensor} is 1000 mm. LLG model results are shown for constant cell thickness of 0.5 mm, by solid (even cell number) and dashed (odd cell number) lines. MC model results are shown for 10 cells, by solid (a and b) and open circles (a only) corresponding to solid and dashed line LLG results respectively. The crossed points at 2 mm thickness in a) are the results of the LLG model for 10 cells and this thickness.

Figure 8: Example use of LLG model to calculate $\overline{\eta}_{beam}$, *QE*, *DQE*, s_{abs}, and *s* as a function of CsI scintillator thickness for a 6 MV beam spectrum. Scintillator cross section was 1.5 by 1.5 mm^2. a) d_{sensor} equals 1 mm. b) d_{sensor} equals 1000 mm.

Figure 1

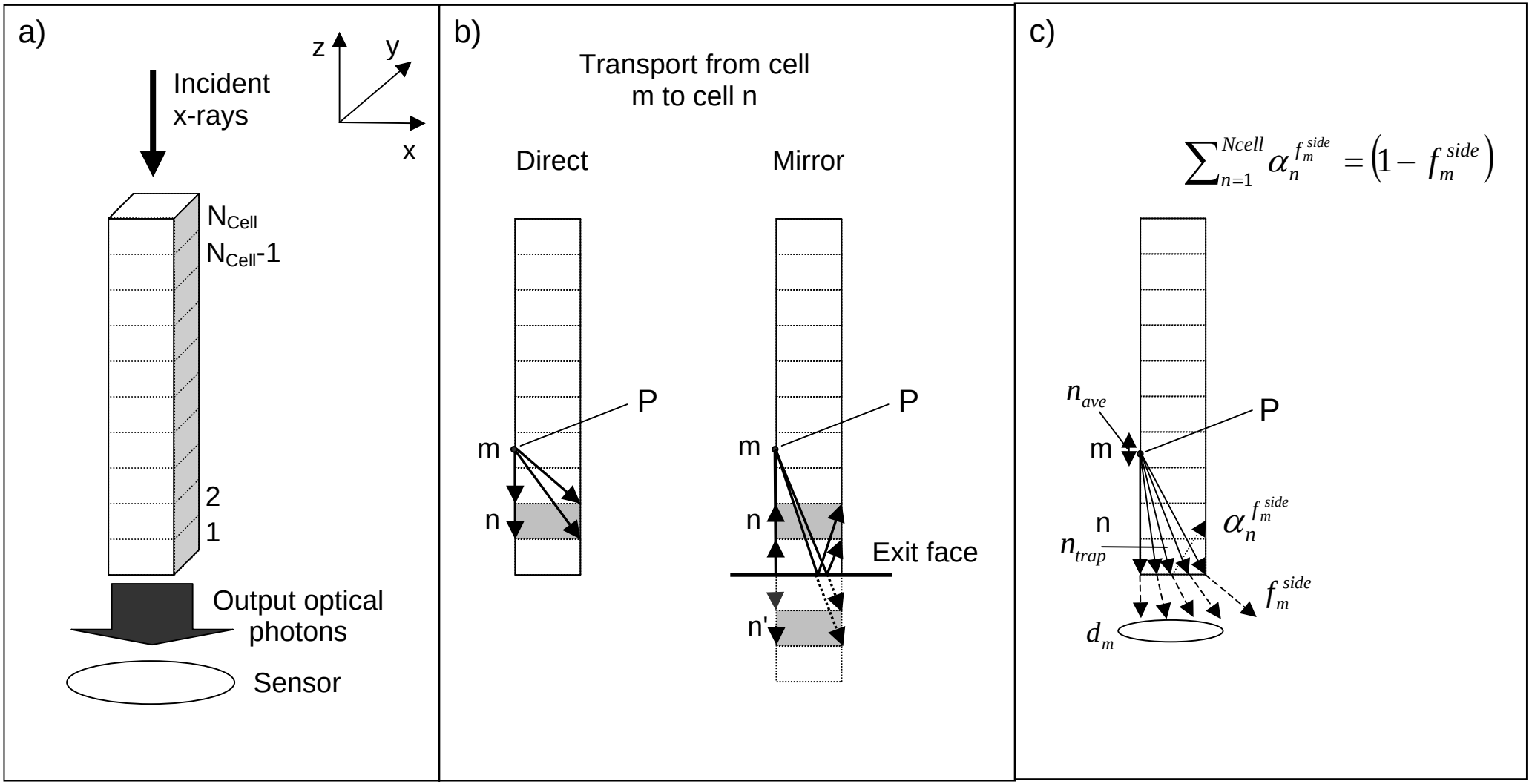
a)
z
y
x
Incident
x-rays
N_{Cell}
N_{Cell}-1
2
1
Output optical
photons
Sensor
b)
Transport from cell
m to cell n
Direct
Mirror
P
m
n
P
m
n
Exit face
n'
c)
$\sum_{n=1}^{Ncell} \alpha_n f_m^{side} = \left(1 - f_m^{side}\right)$
n_{ave}
P
m
n
n_{trap}
$\alpha_n f_m^{side}$
f_m^{side}
d_m

Figure 2

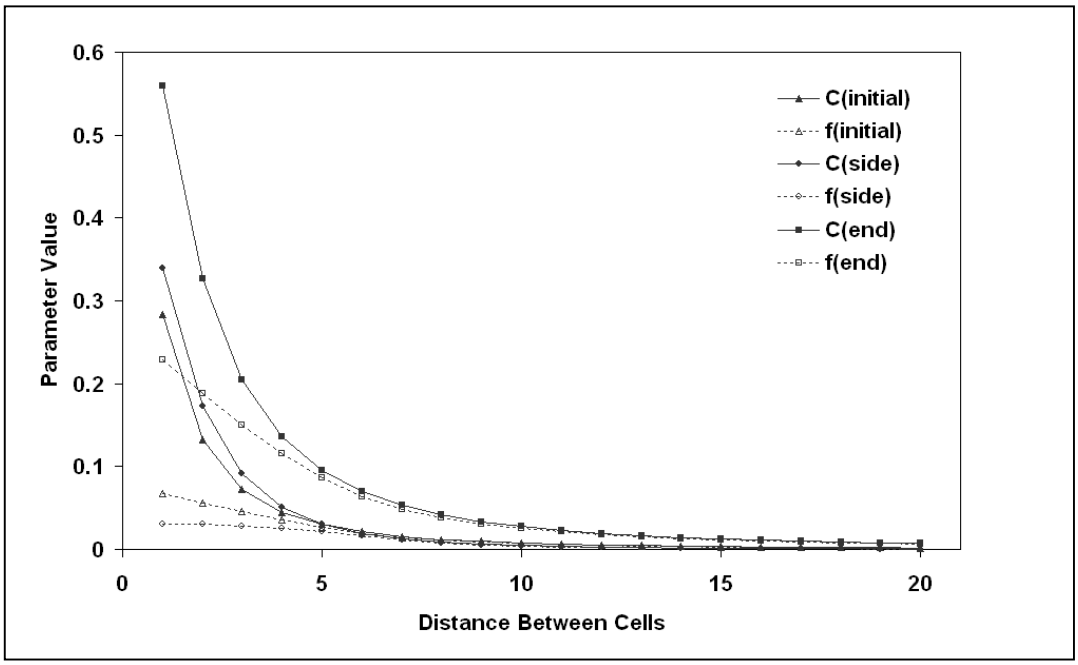
0.6
0.5
0.4
0.3
0.2
0.1
0
Parameter Value
0
5
10
15
20
Distance Between Cells
C(initial)
f(initial)
C(side)
f(side)
C(end)
f(end)

Figure 3

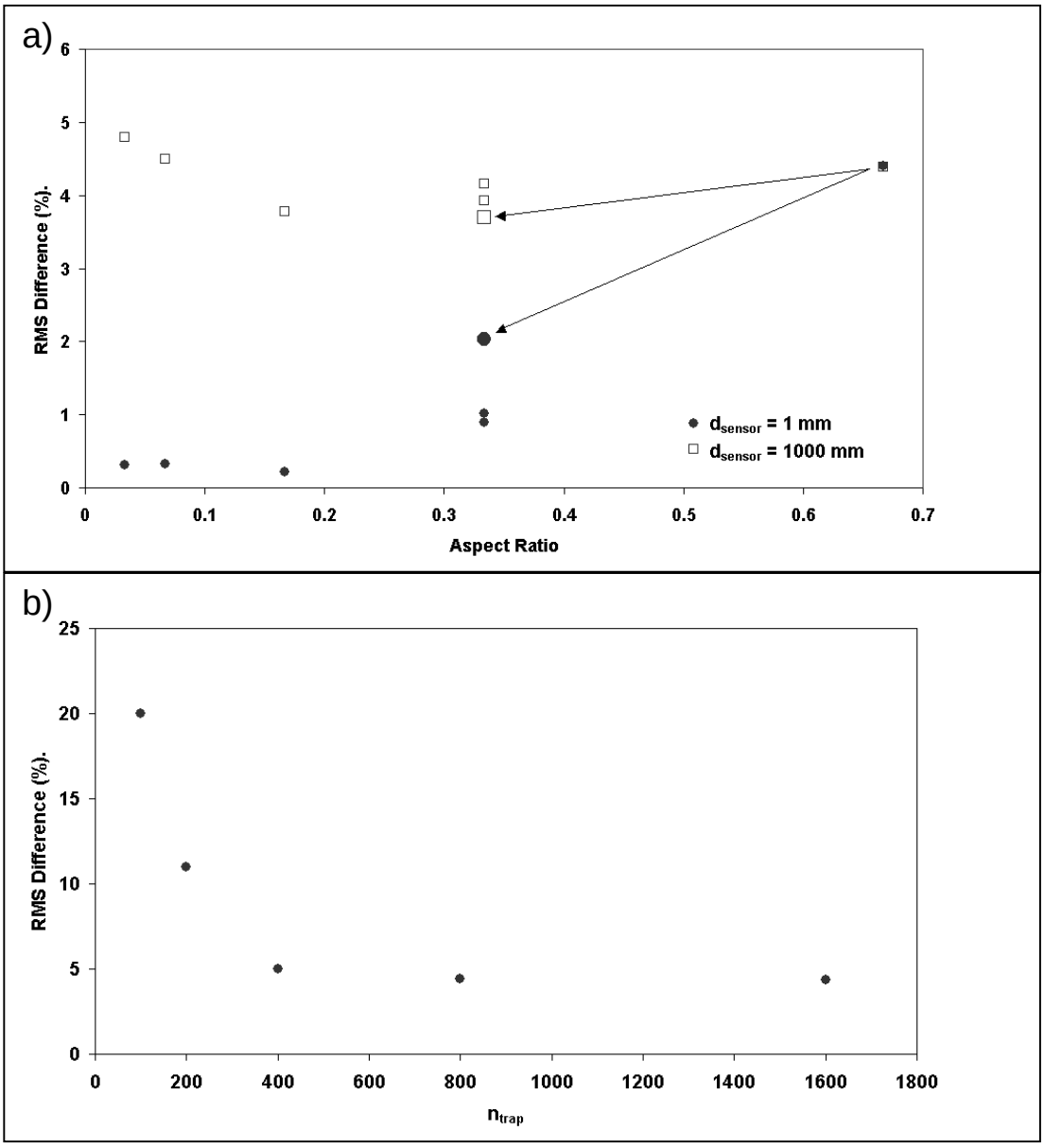
a)
RMS Difference (%).
Aspect Ratio
d_{sensor} = 1 mm
d_{sensor} = 1000 mm
b)
RMS Difference (%).
n_{trap}

Figure 4

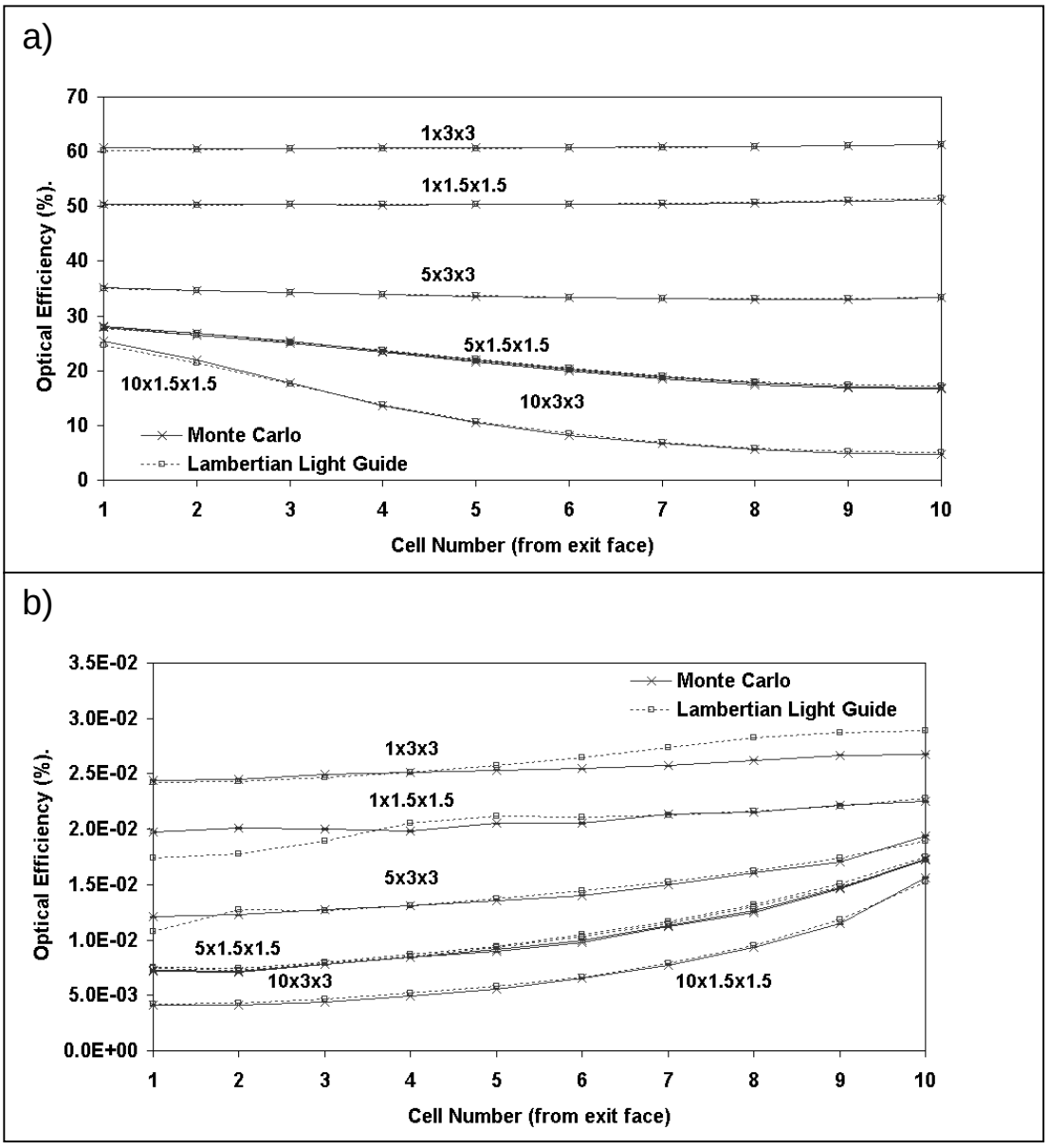
a)
Optical Efficiency (%).
Cell Number (from exit face)
1x3x3
1x1.5x1.5
5x3x3
5x1.5x1.5
10x1.5x1.5
10x3x3
Monte Carlo
Lambertian Light Guide
b)
Optical Efficiency (%).
Cell Number (from exit face)
Monte Carlo
Lambertian Light Guide
1x3x3
1x1.5x1.5
5x3x3
5x1.5x1.5
10x3x3
10x1.5x1.5

Figure 5

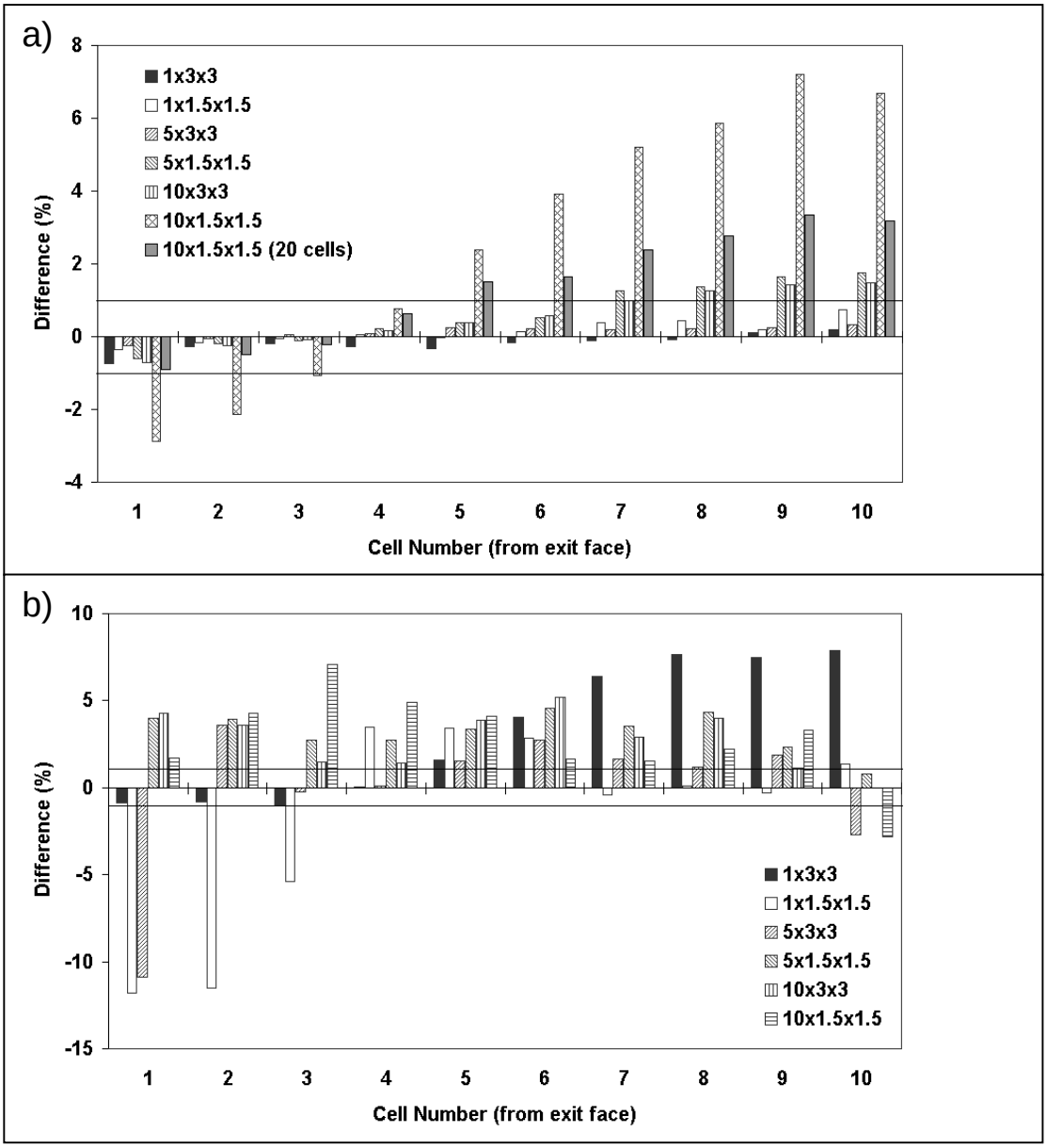
a)
8
6
4
2
0
-2
-4
Difference (%)
1x3x3
1x1.5x1.5
5x3x3
5x1.5x1.5
10x3x3
10x1.5x1.5
10x1.5x1.5 (20 cells)
1
2
3
4
5
6
7
8
9
10
Cell Number (from exit face)
b)
10
5
0
-5
-10
-15
Difference (%)
1x3x3
1x1.5x1.5
5x3x3
5x1.5x1.5
10x3x3
10x1.5x1.5
1
2
3
4
5
6
7
8
9
10
Cell Number (from exit face)

Figure 6

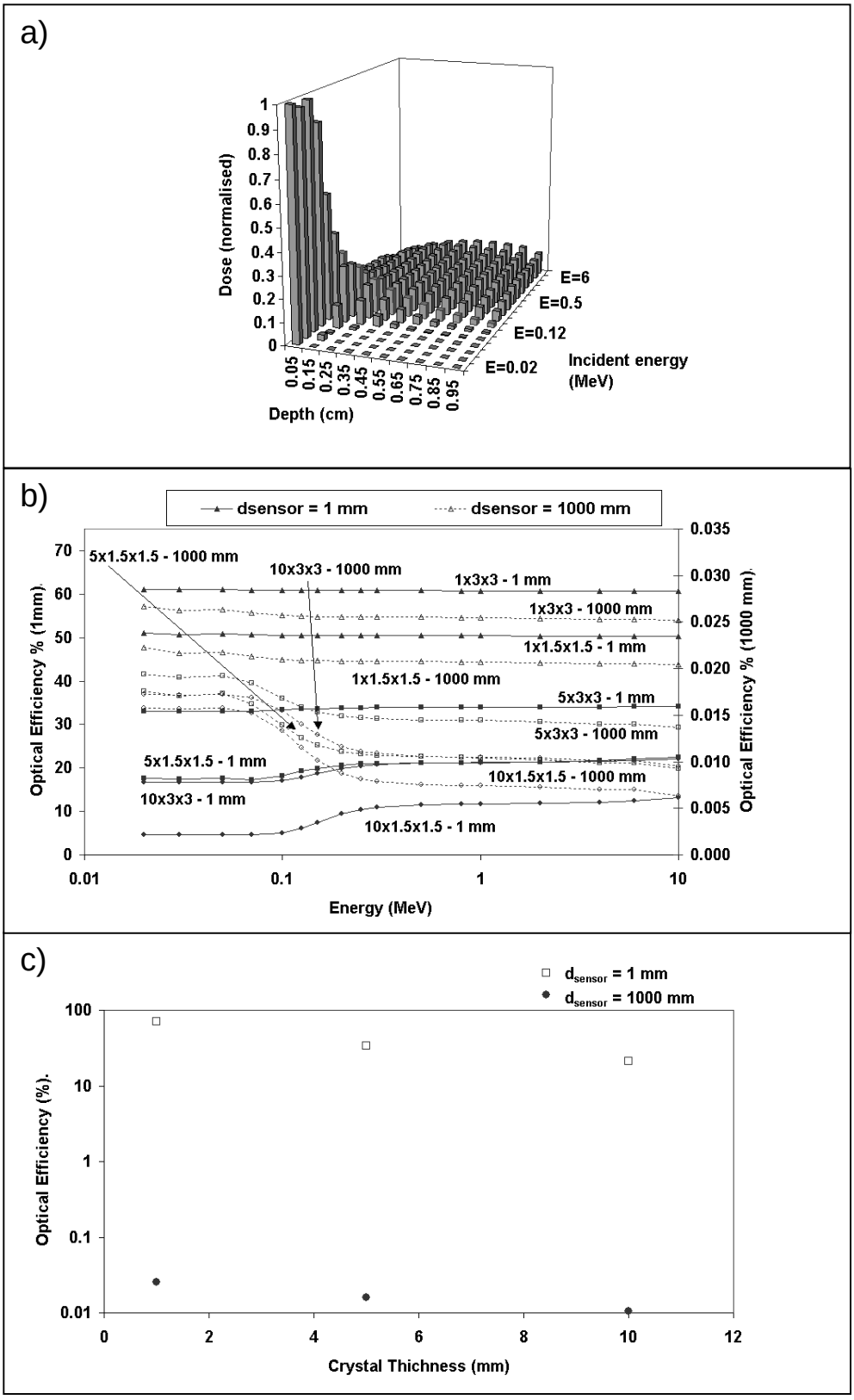
a)
Dose (normalised)
1
0.9
0.8
0.7
0.6
0.5
0.4
0.3
0.2
0.1
0
0.05
0.15
0.25
0.35
0.45
0.55
0.65
0.75
0.85
0.95
Depth (cm)
E=6
E=0.5
E=0.12
E=0.02
Incident energy (MeV)
b)
dsensor = 1 mm
dsensor = 1000 mm
5x1.5x1.5 - 1000 mm
10x3x3 - 1000 mm
1x3x3 - 1 mm
1x3x3 - 1000 mm
1x1.5x1.5 - 1 mm
1x1.5x1.5 - 1000 mm
5x3x3 - 1 mm
5x3x3 - 1000 mm
5x1.5x1.5 - 1 mm
10x1.5x1.5 - 1000 mm
10x3x3 - 1 mm
10x1.5x1.5 - 1 mm
Optical Efficiency % (1mm).
Optical Efficiency % (1000 mm).
70
60
50
40
30
20
10
0
0.035
0.030
0.025
0.020
0.015
0.010
0.005
0.000
0.01
0.1
1
10
Energy (MeV)
c)
d_{sensor} = 1 mm
d_{sensor} = 1000 mm
Optical Efficiency (%).
100
10
1
0.1
0.01
0
2
4
6
8
10
12
Crystal Thichness (mm)

Figure 7

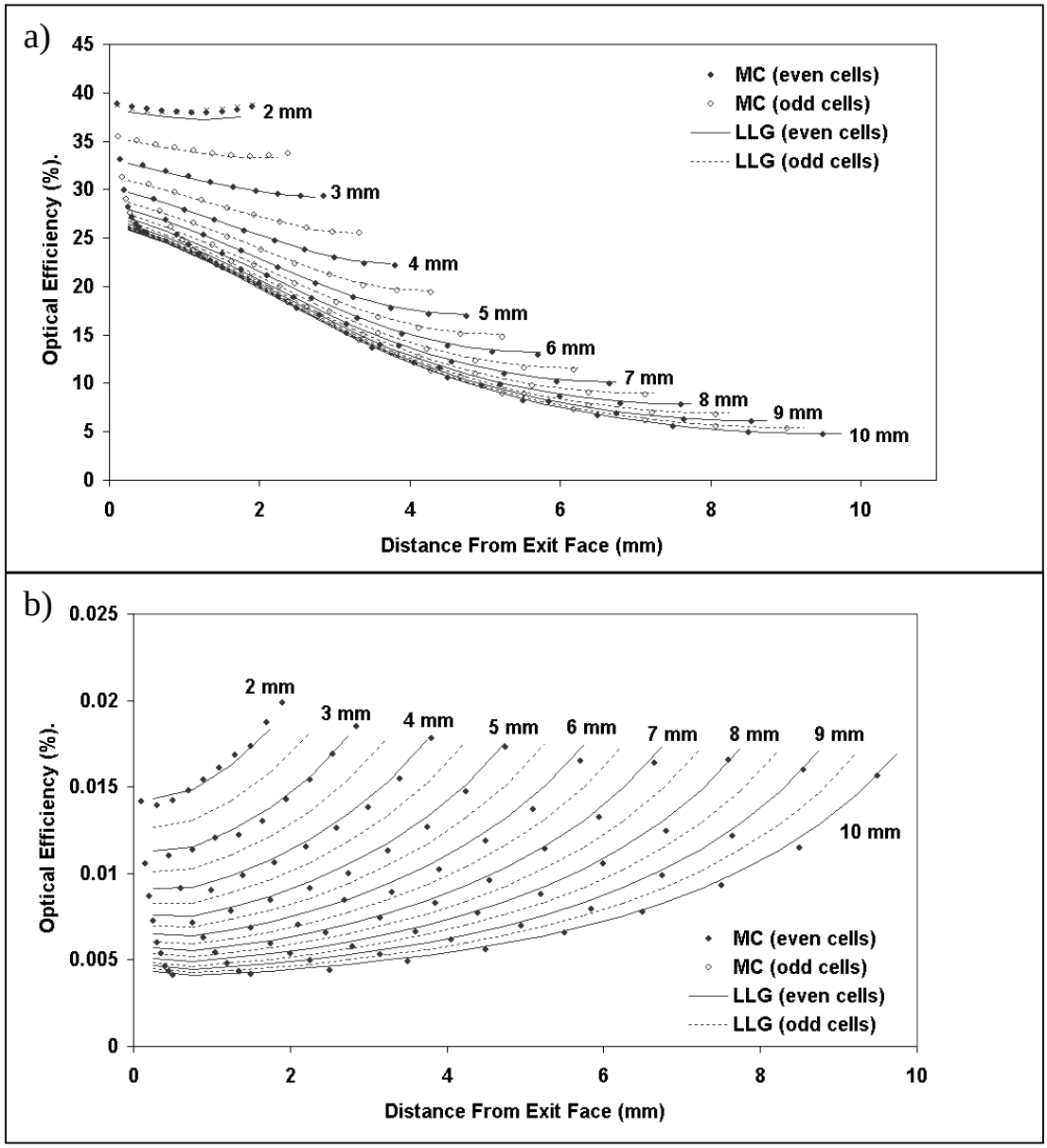
a)
Optical Efficiency (%).
Distance From Exit Face (mm)
MC (even cells)
MC (odd cells)
LLG (even cells)
LLG (odd cells)
2 mm
3 mm
4 mm
5 mm
6 mm
7 mm
8 mm
9 mm
10 mm
b)
Optical Efficiency (%).
Distance From Exit Face (mm)
MC (even cells)
MC (odd cells)
LLG (even cells)
LLG (odd cells)
2 mm
3 mm
4 mm
5 mm
6 mm
7 mm
8 mm
9 mm
10 mm

Figure 8

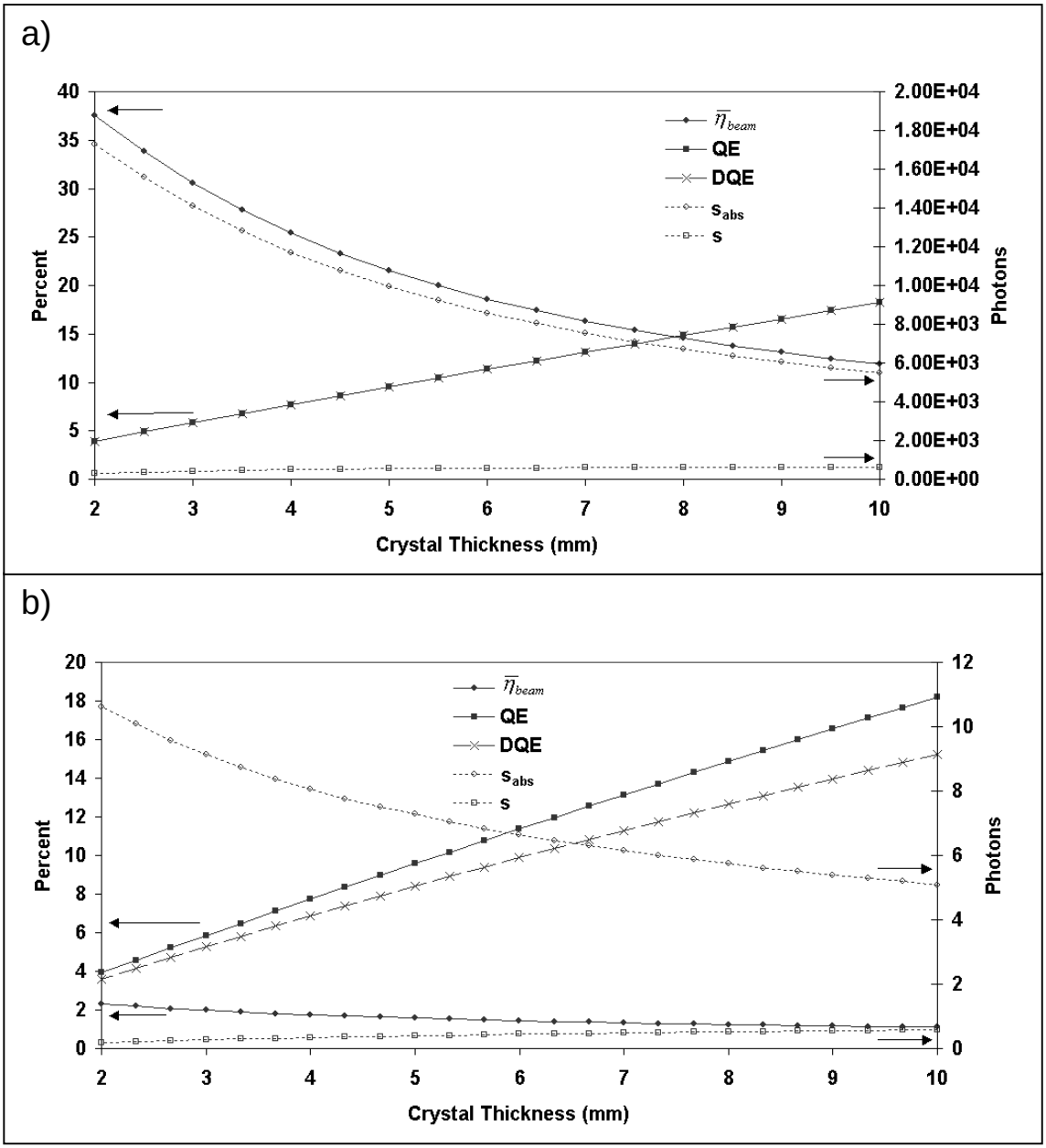
a)
Percent
Photons
Crystal Thickness (mm)
$\overline{\eta}_{beam}$
QE
DQE
s_{abs}
s
b)
Percent
Photons
Crystal Thickness (mm)
$\overline{\eta}_{beam}$
QE
DQE
s_{abs}
s